Chapter 8

The Oscillatory Electrocatalytic Iodate Reduction

8.1 Introduction

The electrochemical reduction of anions such as $S_2O_8^{2-}$, $Fe(CN)_6^{3-}$, $PtCl_4^{2-}$ or CrO_4^{2-} under potentiostatic conditions which were first investigated by Frumkin and co-workers [17, 18, 19] in the early sixties have ever since then remained an active field of research [207, 71, 30, 208, 209].

Their oscillatory instabilities under potentiostatic control [209, 71] can readily be understood by the hypothesis of a Frumkin interaction due to electrostatic repulsion of the electroactive species resulting in a negative impedance [71]. However, under galvanostatic conditions discrepancies arose, as some systems exhibit galvanostatic oscillations, namely IO_3^- and $Fe(CN)_6^{3-}$ in alkaline solution [30, 208, 209] as well as $S_2O_8^{2-}$ in acidic solutions, but others such as $S_2O_8^{2-}$ in alkaline solutions do not. The mechanistic basis of these galvanostatic oscillations has been so far neither satisfactorily understood nor described in terms of numerical models. Despite various suggestions as to the origin of galvanostatic oscillations in general [73, 64, 28, 29], a physically reasonable explanation pertaining to the anion reduction systems was still missing.

Two types of galvanostaticly oscillatory models of the HNDR group have sofar been described in literature (see chapter 7): One comprises the H_2 and the FA oxidation systems and are characterized by (i) a slow chemical species, (ii) a fast chemical species causing the negative impedance and (iii) a current providing process which does not consume any essential species ('independent current carrier').

The other oscillatory HNDR model type originated in work by Koper and Sluyters [64] They pointed out a simple oscillatory two-variable model of the NDR category which exhibited a behavior analogous to systems like the $S_2O_8^{2-}$ reduction in alkaline solutions. These systems have the following features: (i) the double layer potential is the fast autocatalytic species due to an assumed negative impedance, (ii) theses models are unable to show potential oscillations under galvanostatic control and (iii) the major current carrying process consumes the slow chemical species ('dependent current carrier')and (iv) under potentiostatic control the regions of oscillations and

bistability in the (U, R) plane (two-parameter bifurcation diagram) correspond to a XPD (see chapter 2). Koper pointed out that this NDR model can be transformed into a HNDR oscillator, i.e. a system exhibiting galvanostatic potential oscillations, if potential-dependent, non-electrochemical processes such as ad- and desorption of electrochemical species are included (see section 7.4.3). This was found to be associated with a change in shape of the bifurcation diagrams which did no longer exhibit a XPD shape. The latter is a typical feature of an electrochemical oscillator with hidden negative impedance (HNDR oscillator).

As will be concluded in this chapter, neither Koper's HNDR oscillator subclass nor the HNDR subclass containing the FA/ hydrogen oxidation systems are able to adequately describe the galvanostatic behavior of systems like the iodate reduction. Instead, the experimental and theoretical investigation of the latter system will lead to the suggestion of an additional third oscillatory subclass within the HNDR category. Apart from iodate, systems such as the oscillatory galvanostatic $Fe(CN)_6^{3-}$ reduction or the $Fe(CN)_6^{4-}$ oxidation will turn out to belong to this new class.

The organization of this chapter is as follows: After an experimental characterization of the iodate reduction system, a detailed chemical reaction mechanism leads to the formulation of a dimensionless system of evolution equations. An analytical and numerical analysis of the model reveals dynamical features which compare favorably with those of the experimental system. In addition, the model allows the study of the changes in the bifurcation structure occurring during a continuous transition between a NDR and HNDR oscillator model. The subsequent mechanistic discussion of the introduced model also addresses previously suggested instability mechanisms for the iodate system.

8.2 Experimental

A polished Ag wire (area: 0.3 cm^2), a Pt-wire and a Hg/Hg_2SO_4 electrode were employed as working, counter and reference electrode, respectively. All experimental potentials reported in this chapter refer to the Saturated Calomel Electrode (SCE). The electrolyte solutions contained 0.15 M or 0.05 M $NaIO_3$ (Merck, p.a.) as well as 1M $NaOH$ (puriss.p.a., Fluka) as supporting electrolyte and were freshly prepared prior to measurements. All chemicals were employed without further purification. Steady N_2 bubbling (5N) of the electrolyte ensured the absence of oxygen during the entire experimental procedures.

The frequency range of the impedance measurements reached from 10 kHz to 0.01 Hz with the number of measurements points per frequency decade varying from 10 to 25.
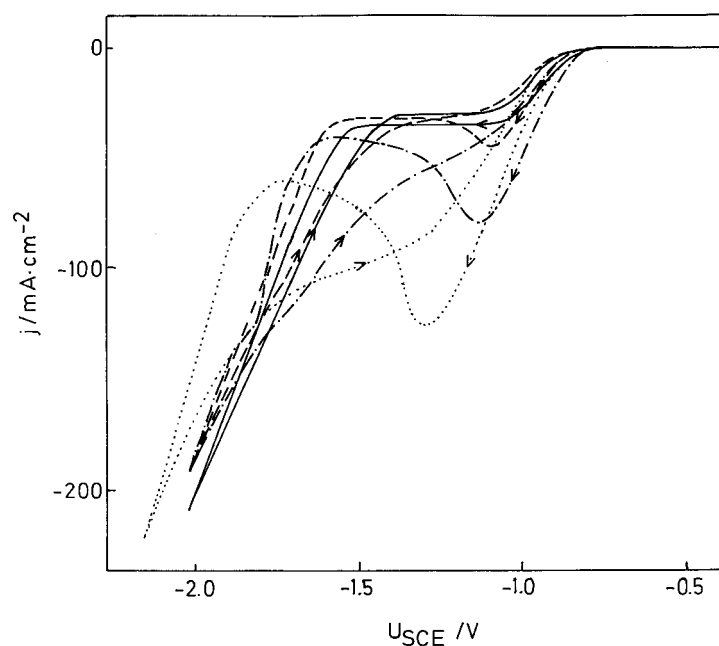
Figure 8-1: Experimental cyclic voltammetric profiles of iodate reduction on Ag in alkaline solution (0.15 M $NaIO_3$, 1 M $NaOH$) at various scan rates. solid: 2mV/s, dashed: 10 mV/s, dot-dashed: 50 mV/s, dotted: 200 mV/s.

8.3   Results

8.3.1   Experimental Characterization

Cyclic Voltammetry

The I/U behavior of the iodate system at various potential scan rates is illustrated in Fig.8-1. At 2 mV/s a quasi-stationary, diffusion-limited current plateau was observed in both scan directions due to mass-transport controlled iodate reduction followed by a steep current increase due to hydrogen evolution (gas bubbles!). At higher scan rates, strongly asymmetric CVs were obtained. On the cathodic scan, the fast increase in overpotential leads to a sharp decrease of iodate at the interface evidenced by the N-shaped voltammetric profile. After recovery of the iodate concentrations due to convection (gas bubbling), the current values on the reverse scan are initially higher than those on the cathodic scan.

Fig. 8-2 and 8-3 shows the system behavior upon current scanning for two different iodate concentrations. A 'hard' transition from stable to oscillatory behavior is seen at low absolute values of j, whereas a soft supercritical Hopf bifurcation is discerned at high j. The oscillation period seems to be inversely correlated with the iodate bulk concentration, as typically found in systems where the rate of diffusive mass-transport between bulk and surface is an essential part of the oscillatory dy-
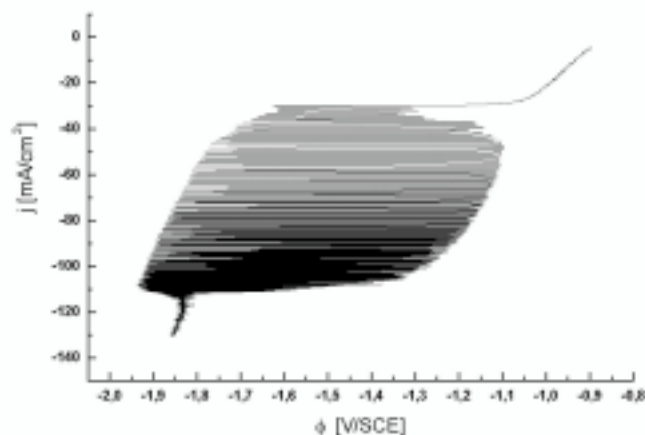
Figure 8-2: Experimental I/U behavior during current scans (0.05 mA/s) in the absence of stirring, 1 M $NaOH$, 0.15 M $NaIO_3$.

namics. The potentials observed at currents right above and below of the oscillatory region correspond to reduction of iodate and water (hydrogen evolution), respectively. Finally, Fig. 8-4 portrays a stationary time series at $I = -17\ mA$ without stirring. Upon stirring (arrow), the oscillations cease and the potential settles to a stationary high value. This behavior is easily understood if one recalls that stirring increases the diffusion-limited current of iodate such that the chosen total current can entirely be provided by iodate reduction at high potentials. Thereby, the oscillatory current range beyond the diffusion-limited plateau is shifted to higher current values. Beyond a critical stirring rate all potential oscillations completely disappeared.

Impedance Studies

In Fig. 8-5 through Fig. 8-8, the results of a potentiostatic impedance analysis of the iodate system are reported in the Nyquist representation. At $U = -1.06\ V$ (Fig. 8-5) the frequency-dependent impedance reveals two capacitive loops indicating a stable electrochemical system with two chemical processes on different time scales. At lower potentials (Fig. 8-6, $U = -1.26\ V$), the shape of the impedance plot changes drastically. The low-frequency capacitive loop disappears in favor of an inductive one and extrapolation suggests the presence of a negative real impedance (equivalent to a NDR) at $\omega = 0$. At $U = -1.56\ V$ (Fig. 8-7) a hidden negative impedance is observed since Re Z is negative on a finite frequency range only. Finally, at a potential where the hydrogen current prevails ($U = -1.66\ V$, Fig.8-7) the real part of the impedance no longer shows a negative value; instead, the high-frequency capacitive loop dominates followed by a smaller inductive one.
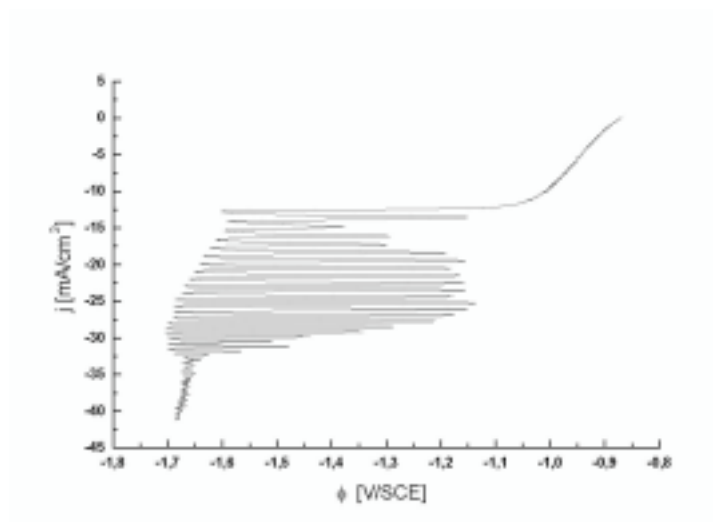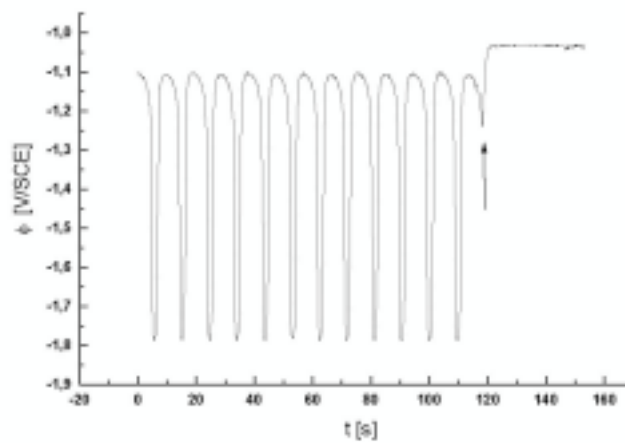
Figure 8-3: Experimental I/U behavior during current scans (0.05 mA/s) in the absence of stirring, 1 M $NaOH$, 0.05 M $NaIO_3$.
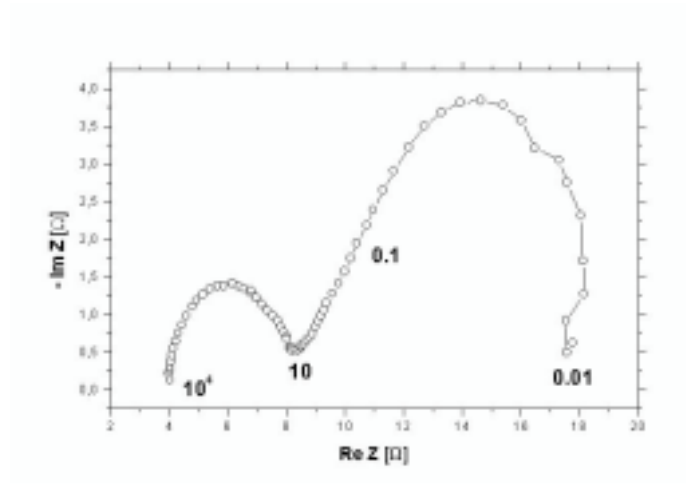
Figure 8-5: Impedance behavior of the experimental iodate system illustrated in terms of Nyquist diagrams at various potentials, frequency range 10 kHz - 0.01 Hz, $U = -1.06$ *V.*
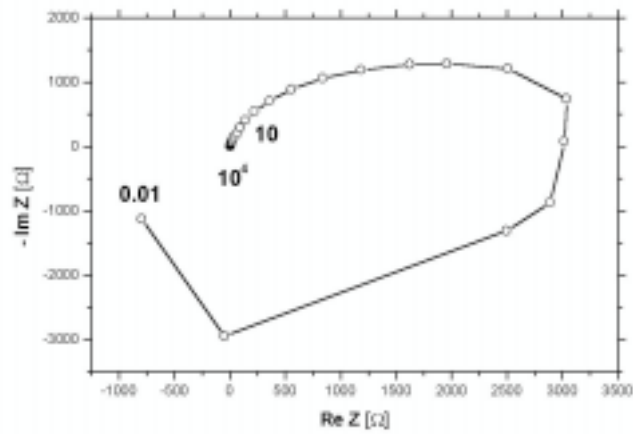
Figure 8-7: Impedance behavior of the experimental iodate system illustrated in terms of Nyquist diagrams at various potentials, frequency range 10 kHz - 0.01 Hz, $U = -1.56$ V.
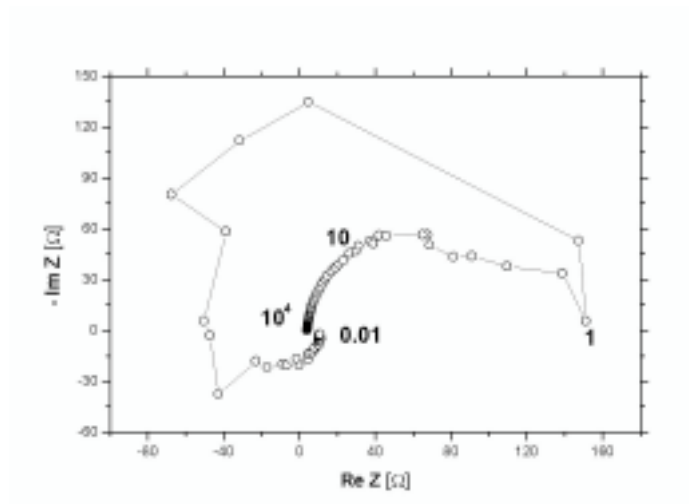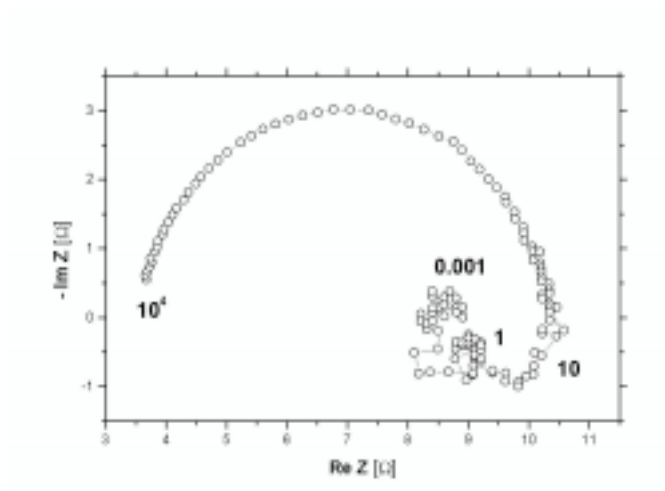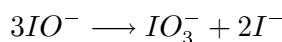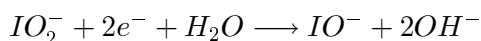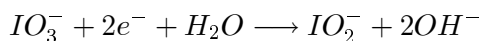
8.3.2 Model Calculations

The Chemical Reaction Mechanism

General iodate chemistry. In a strongly alkaline solution IO_3^- -ions are known to undergo a stepwise electrocatalytic reduction to IO^- via the reactive intermediate IO_2^- followed by a disproportionation reaction yielding I^- and IO_3^- [210]:

$$IO_3^- + 2e^- + H_2O \longrightarrow IO_2^- + 2OH^-$$

$$IO_2^- + 2e^- + H_2O \longrightarrow IO^- + 2OH^-$$

$$3IO^- \longrightarrow IO_3^- + 2I^-$$

I_2 forms, if at all, in small traces only and immediately disproportionates into I^- and IO^- :

$$2IO^- + 2e^- + 2H_2O \longrightarrow I_2 + 4OH^-$$

$$I_2 + 2OH^- \longrightarrow I^- + IO^- + H_2O \ .$$
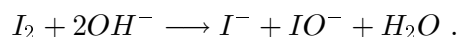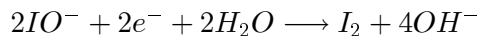
I^-, on the other hand, is unable to undergo any comproportionation reaction. Thus, as the electrochemical reaction proceeds, IO_3^- is essentially reduced to I^- which constitutes the final inert product[210].

Model mechanism. Consider the diffusive mass transport of the electroreactive species between the bulk and the electrode

$$IO_{3\,bulk}^- \rightleftarrows IO_{3\,dl}^-, \tag{8.1}$$

followed by the potential-dependent reduction of $IO_{3\,dl}^-$ to some inert, non-adsorbed product P, e.g. I^-:

$$IO_{3\,dl}^- + n\,e^- \longrightarrow P \tag{8.2}$$

Here, $IO_{3\,bulk}^-$ and $IO_{3\,dl}^-$ denote the concentration of IO_3^- in the bulk and respectively right outside the double layer.

The latter reaction is assumed to proceed without any adsorbed intermediates. Its functional dependence on potential strongly determines the overall system dynamics. Similar to electrochemical reduction reactions of anions such as $S_2O_8^{2-}$ [71] , a Frumkin-type coulomb interaction between the electroactive species within the diffusive double layer will be assumed to operate during reaction 8.2 over some potential interval. This assumption is justified for reduction (oxidation) of highly charged electroactive anions (cations) around the point of zero charge.

As suggested by the experimental findings, apart from the IO_3^- reduction reaction, the electrocatalytic reduction of protons are to be considered as an *additional current*

providing chemical process. The potential-dependent reaction sequence reads

$$* + H_2O + e^- \rightleftharpoons H_{ad} + OH^- \tag{8.3a}$$

$$H_{ad} + H_2O + e^- \longrightarrow H_2 + OH^- \tag{8.3b}$$
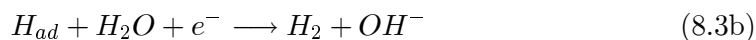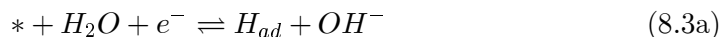
with the second step being rate-determining on Pt and Au electrodes [63]. $*$ denotes a bare surface site and H_{ad} represents atomically adsorbed hydrogen. The concentration of H_{ad} can safely be eliminated adiabatically [63] which leads, in the absence of any other adsorbed species and assuming a constant concentration of protons, to a merely potential-dependent rate law for the hydrogen evolution reaction. Note that in ref. [49] step 8.3a is reported to be slower than step 8.3b for Au and Ag in acidic electrolytes. However, this would imply a negligible surface coverage of H_{ad} and hence again result in a merely potential-dependent hydrogen current. In contrast, in the presence of an additional surface species,e.g. θ_2, the rate expression becomes explicitly dependent on the number of bare surface sites $(1 - \theta_2)$.

Eq. 8.1, 8.2 and 8.3 with $n = 6$ are henceforth referred to as mechanism A. Compared to previous electrochemical models for oscillatory reactions [71, 64] mechanism A involves an additional current-providing reaction which will add interesting new dynamics.

As for reaction 8.2 it is arguable whether it is physically reasonable that the electron transfer of six electrons is simply lumped into one single step. Therefore, an extended mechanism B considers a stepwise reduction of IO_3^- to I^- according to the following scheme:

$$IO_{3\,dl}^- + n\,e^- \longrightarrow X \tag{8.4a}$$

$$X + m e^- \longrightarrow P \tag{8.4b}$$

Here, X denotes a chemical intermediate, e.g. IO_2^- or IO^- , formed by the initial reduction of IO_3^- , followed by the potential-dependent consumption of X to form the final inert product P, i.e. I^-. As long as eq. 8.4a is rate determining, X can be eliminated adiabatically so that mechanism A is essentially recovered.

The Galvanostatic Model

For the purpose of a concise, yet realistic mathematical formulation of mechanism A, we have to identify the dynamical species (variables) which are 'essential' for the chosen chemical mechanism [33] under experimental conditions. Since we are focusing on bistability and limit cycle behavior, we chose two chemical species out of mechanism A: first, the iodate concentration at the double layer and, second, the double layer potential ϕ. In contrast to the iodate reduction current, the hydrogen evolution constitutes an additional iodate-'independent' current carrier (subscript 'icc'), i.e. it gives rise to a current which does not consume the essential species iodate. Making use of the Nernst diffusion layer approximation [71, 64, 72, 211], i.e. assuming an instantaneous linear concentration profile within the mass transport boundary layer near the electrode, and modelling the evolution of ϕ by a simple charge balance equation, the dimensional evolution equations of the species of model

A read

$$\dot{c} = \frac{dc}{dt} = \frac{2D}{\delta^2}\left(c_b - c\right) - \frac{2}{\delta}\, c\, k_r^0\, k_r(\phi, k_1^0) \tag{8.5a}$$

$$C\dot{\phi} = C\frac{d\phi}{dt} = J_{tot} + n_1 F c\, k_r^0\, k_r(\phi, k_1^0) + n_2\, k_{icc}^{00}\, \widetilde{k}_{icc}(\phi). \tag{8.5b}$$

Here, c denotes the iodate concentration at the double layer, $IO_{3\,dl}^-$, ϕ the double layer potential, F the Faraday constant, C the interfacial capacitance, D and c_b the diffusion constant and the bulk concentration of IO_3^- and δ the diffusion layer thickness. Furthermore, J_{tot}, n_1 and n_2 represent the total current density and the number of electrons transferred in reaction 8.2 and 8.3, respectively. Finally, while k_r^0 and k_{icc}^{00} are dimensional rate constants, $k_r(\phi, k_1^0)$ and $\widetilde{k}_{icc}(\phi)$ are Butler-Volmer-type exponential expressions describing the potential-dependence of the rate of iodate reduction (eq. 8.2) and of hydrogen evolution (eq. 8.3), respectively. Obviously, the second and third term in eq. 8.5b take care of the individual contributions of the iodate reduction and the hydrogen evolution to the total current. As pointed out before, due to the adiabatic elimination of H_{ad} - taking the equilibrium constant of eq. 8.3a to be K_{eq}, it follows $H_{ad} = \frac{K_{eq}}{[OH^-]+K_{eq}}$ - and due to the absence of any other surface species, the rate of hydrogen evolution does not depend explicitly on the number of bare surface sites, but is purely potential-dependent.

Recasting eq.8.5 in a dimensionless form one obtains

$$\dot{c}' = a\left(1 - c'\right) - c'\, k_r(\phi', k_1^0) \tag{8.6a}$$

$$\epsilon\, \dot{\phi}' = I + c'\, k_r(\phi', k_1^0) + k_{icc}^0\, \widetilde{k}_{icc}(\phi'). \tag{8.6b}$$

where

$$I = \frac{J_{tot}}{n_1 F c_b\, k_r^0}\;; \epsilon = \frac{2CRT}{\delta n_1 F c_b}; \phi' = \frac{\phi}{1V}; c' = \frac{c}{c_b}; a = \frac{D}{\delta\, k_r^0};$$

$$k_{icc}^0 = \frac{n_2\, k_{icc}^{00}}{n_1 c_b k_r^0}; \tau = \frac{2}{\delta}k_r^0 t$$

Model eq. 8.6 involves five system parameters three of which, the total current I as well as rate constants k_{icc}^0 and k_1^0 , will be used as bifurcation parameters in the following section. Henceforth all primes will be dropped.

Next, the functional forms of the potential-dependent terms need to be specified. While $\widetilde{k}_{icc}(\phi)$ was chosen to be a usual Butler-Volmer term according to

$$\tilde{k}_{icc}(\phi) = e^{-\alpha f\,(\phi - \phi_0)}$$

the expression $k_r(\phi', k_1^0)$ was associated with the N-shaped function [64]:

$$k_r(\phi, k_1^0) = k_1^0 \, e^{-\alpha f \, \phi} + \frac{e^{-\alpha f \, \phi}}{1 + 250 \, e^{- \, f \, (\phi - \phi_0)}}.$$

(Strictly speaking it is a mirror-imaged N-shape, but we will not distinguish between them).The parameter ϕ_0 means an arbitrary standard potential , $f = F/RT$ and α denotes the symmetry factor. The shape of $k_r(\phi', k_1^0)$ was chosen in order to mimic a Frumkin-type double layer effect which usually leads to a negative regulation between double layer potential and reaction rate resulting in a negative slope in the I/ϕ characteristics (NDR) [48, 64, 71, 63].

It should be kept in mind that the galvanostatic numerical models can be transformed into the respective potentiostatic ones by simply replacing I by $\frac{U - \phi}{\rho}$ with ρ and U denoting a dimensionless resistance and the externally applied constant potential, respectively.

Linear stability analysis

Here it is shown that the Hopf bifurcation conditions can be fulfilled in eq.8.6 owing to the chosen potential dependences of both current carriers.

Given the galvanostatic system equations

$$\dot{c} = a \, (1 - c) - \, c \, k_r(\phi, k_1^0)$$

$$\epsilon \, \dot{\phi} = I + c \, k_r(\phi, k_1^0) + k_{icc}^0 \widetilde{k}_{icc}(\phi)$$

its Jacobian matrix at a stationary reference state (c_{ss}, ϕ_{ss}) reads (subscripts 'ss' is dropped)

$$J = \begin{pmatrix} -a - k_r(\phi, k_1^0) & -c \frac{\partial k_r(\phi, k_1^0)}{\partial \phi} \\ \frac{k_r(\phi, k_1^0)}{\epsilon} & \frac{c}{\epsilon} \frac{\partial k_r(\phi, k_1^0)}{\partial \phi} + \frac{k_{icc}^0}{\epsilon} \frac{\partial \widetilde{k}_{icc}(\phi)}{\partial \phi} \end{pmatrix}.$$

If the parameters are chosen such that $k_r(\phi, k_1^0)$ exhibits an inverse regulation, i.e. $\frac{\partial k_r(\phi, k_1^0)}{\partial \phi} > 0$, while $\frac{\partial \widetilde{k}_{icc}(\phi)}{\partial \phi}$ shows normal reductive regulation, i.e. $\frac{\partial \widetilde{k}_{icc}(\phi)}{\partial \phi} < 0$, it follows for the trace and the Determinant of J

$$TrJ = \underbrace{-a - k_r(\phi, k_1^0)}_{<0} + \underbrace{\frac{c}{\epsilon} \frac{\partial k_r(\phi, k_1^0)}{\partial \phi}}_{>0} + \underbrace{\frac{k_{icc}^0}{\epsilon} \frac{\partial \widetilde{k}_{icc}(\phi)}{\partial \phi}}_{<0}$$

$$DetJ = \underbrace{-a \frac{c}{\epsilon} \frac{\partial k_r(\phi, k_1^0)}{\partial \phi}}_{<0} \underbrace{-a \frac{k_{icc}^0}{\epsilon} \frac{\partial \widetilde{k}_{icc}(\phi)}{\partial \phi}}_{>0} \underbrace{-k_r(\phi, k_1^0) \frac{k_{icc}^0}{\epsilon} \frac{\partial \widetilde{k}_{icc}(\phi)}{\partial \phi}}_{>0}$$
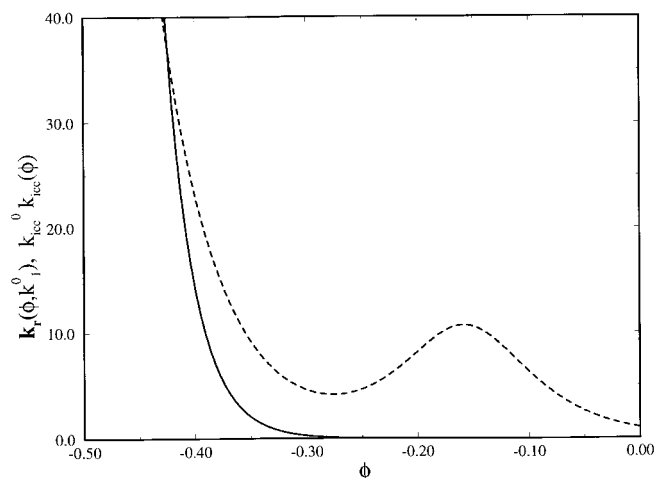
Figure 8-9: Potential dependence of the rate expressions of IO_3^- reduction , $k_r(\varphi, k_1^0)$ (dashed), as well as of hydrogen evolution, $k_{icc}^0 \widetilde{k}_{icc}(\varphi)$ (solid), for $k_1^0 = 0.01, k_{icc}^0 = 0.3$.

According to the Routh-Hurwitz criterion [212, 176] a Hopf bifurcation occurs in a two-variable system, if the conditions $TrJ = 0 \wedge DetJ > 0$ are fulfilled. One can show that these conditions can simultaneously be met owing to positive and negative terms in the Determinant. It is obvious from the expression for the determinant, that it is the additional current carrier (H_2 evolution) which enables the galvanostatic limit cycle behavior since it does not consume the slow chemical species.

Numerical Analysis

In this section the dynamical behavior of the iodate model under both potentiostatic and galvanostatic conditions will be investigated. Throughout this section the parameters a, ϵ, α, f and ϕ_0 will be fixed at the following values: $a = 1, \epsilon = 0.3, \alpha = 0.5, f = 38.7$ and $\phi_0 = -0.3$. The remaining parameters are indicated in the Figures. Bifurcation behavior was calculated with the continuation package AUTO [109], numerical integration was performed using the lsode package [108]

1. Potential dependence of the current carriers Fig.8-9 portrays the potential dependence of the reaction rates of the IO_3^- reduction ($k_r(\phi, k_1^0)$, dashed) and hydrogen evolution ($k_{icc}^0 \widetilde{k}_{icc}(\phi)$, solid) for a typical set of parameters $k_1^0 = 0.01, k_{icc}^0 = 0.3$. Clearly visible is the negative, inverse regulation of $k_r(\phi, k_1^0)$ over some potential interval where the reaction rate decreases with an increase in absolute overpotential. The function $k_{icc}^0 \widetilde{k}_{icc}(\phi)$, on the other hand, is characterized by a usual Butler-Volmer-type exponential shape with purely positive regulation. Note that the hydrogen reaction rate outweights $k_r(\phi, k_1^0)$ at low potentials in agreement with experimental findings.
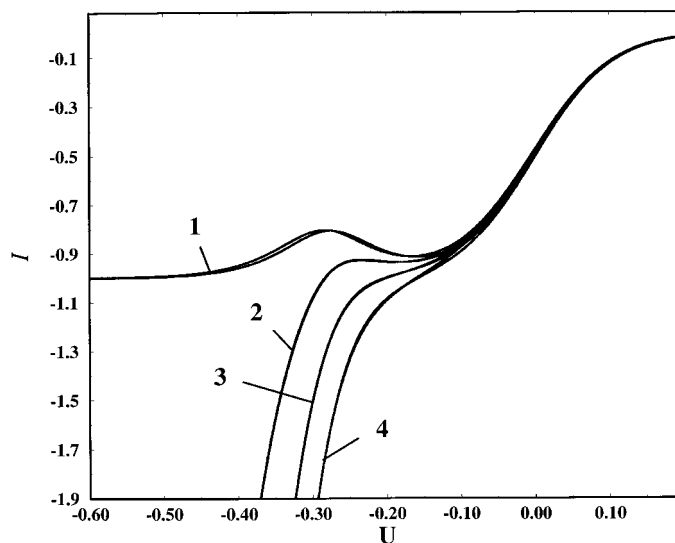
Figure 8-10: Calculated, quasi-stationary, voltammetric profiles of model A at scan rate 0.002 for different values of k_{icc}^0, $k_1^0 = 0.01, \rho = 0.005, U_{initial} = +0.3, U_{turn} = -0.7.$ 1: $k_{icc}^0 = 0.0$, 2: $k_{icc}^0 = 0.3$, 3: $k_{icc}^0 = 0.8$, 4: $k_{icc}^0 = 1.5$.

2. The voltammetric behavior The quasi-stationary I/U behavior of model A upon varying the rate constant of hydrogen evolution, k_{icc}^0, is shown in Fig.8-10. As the contribution of the hydrogen evolution to the total current is increased, the effect of the inverse potential regulation of $k_r(\phi, k_1^0)$, visible in curve 1 and 2 as a region of negative differential resistance, is completely compensated for by the positive regulation of $k_{icc}^0 \widetilde{k}_{icc}(\phi)$ (curve 3 and 4) and becomes hidden. Still, for parameters of curve 3 and 4 the system exhibits both potentiostatic current oscillations at higher values of the resistance and galvanostatic potential oscillations as will be seen later on. While curves 1 and 2 represent the situation where the iodate model is of the NDR oscillator type, the latter I/U curves are commonly found in galvanostatic oscillatory models of the HNDR type [26, 74, 23, 27, 72]. Thus, Fig.8-10 depicts the continuous transition from a NDR to a HNDR oscillator by increasing the contribution of an additional current carrier which does not consume the major electrochemical species. Fig.8-11 allows for a more detailed analysis of the individual contributions of iodate and hydrogen evolution to the overall current. Note that the N-like shape of the CV becomes more pronounced at higher scan rates compared to curve 2 in Fig.8-10 since aside from the negative potential regulation the mass depletion of IO_3^- at the double layer becomes effective. Even in the absence of a negative impedance on the stationary polarization curve ($k_{icc}^0 = 1.5$), the mass depletion at the surface can pretend a negative I/U regulation at finite scan rates as shown in Fig.8-12.

While dynamical instabilities are not visible in the potential scans due to small values of ρ, galvanostatic current scans (Fig.8-13) reveal a current range of stable
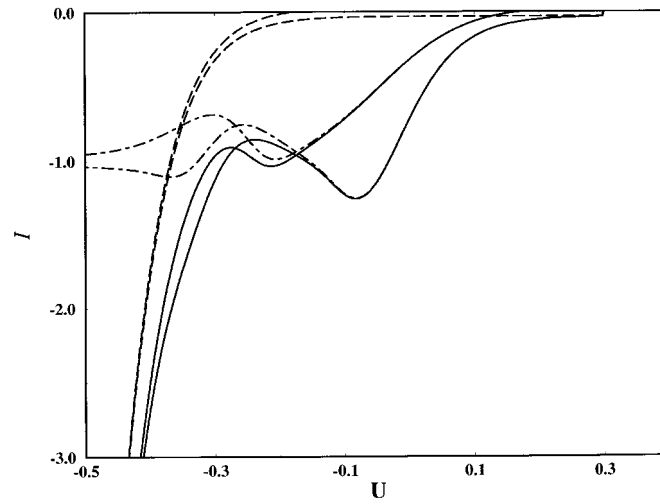
Figure 8-11: Numerical CVs of eq.8.6 at scan rate 0.1, $\rho = 0.005, U_{initial} = +0.3, U_{turn} = -0.7$, solid line: full model, $k_{icc}^0 = 0.3, k_1^0 = 0.01$; dotted-dashed line: IO_3^- reduction current only, $k_{icc}^0 = 0.0, k_1^0 = 0.01$; dashed line: hydrogen evolution current only, $k_r(\varphi, k_1^0) = 0.0, k_{icc}^0 = 0.3$.
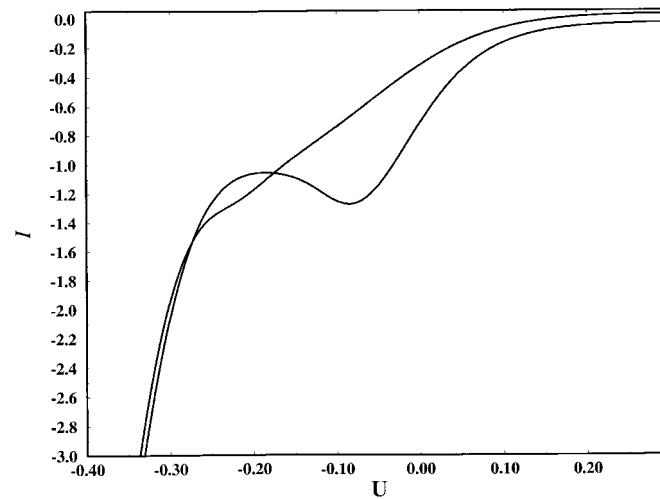

Figure 8-12: I/U characteristics of model A at large k_{icc}^0 upon fast scanning, scan rate=0.1, $\rho = 0.005, U_{initial} = +0.3, U_{turn} = -0.7, k_{icc}^0 = 1.5, k_1^0 = 0.01$.
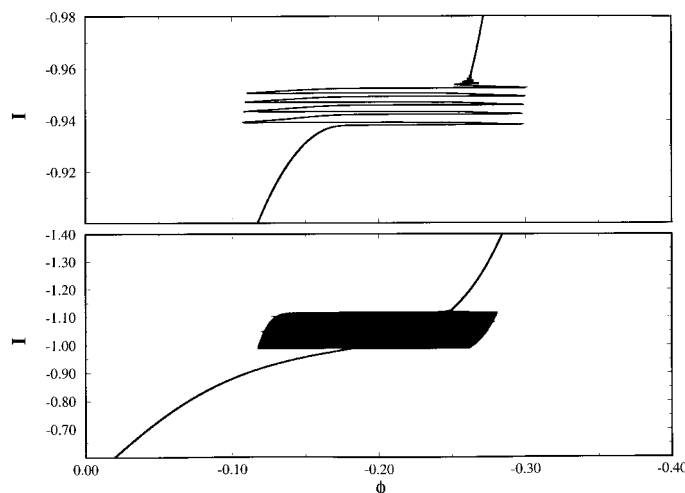
Figure 8-13: I/U profiles of model A upon galvanostatic current scanning, scan rate=0.001 , $k_1^0 = 0.01, k_{icc}^0 = 0.3$ (upper graph) and 0.8 (lower graph), $I_{initial} = -0.4, I_{final} = -1.4$.

limit cycle behavior. The exact nature of the transitions between stable and limit cycle behavior is revealed using numerical continuation methods [109] which provide solution curves of stationary states and limit cycles as displayed in Fig.8-14. The calculated galvanostatic behavior is to be compared with experimental results in Fig.2 a,b and with those in Fig.5 a,b of ref.[30].

3. Impedance diagrams In analogy to experiments, the frequency responses of the model were calculated [74, 23] at various stationary points (Fig.8-15 to Fig. 8-18). The comparison with findings of Fig. 8-5 to Fig. 8-8 evidences agreement of model and experiment as far as the presence of a frequency range with negative impedance is concerned. Corresponding experimental impedance plots were also reported in the electrochemical reduction of $Fe(CN)_6^{3-}$ in ref. [208, 209].

4. Galvanostatic bifurcation behavior Next, various diagrams are reported which illustrate the dynamical regimes as well as the bifurcation of model A in dependence of two parameters. Fig.8-19 and 8-20 portray the behavior of the galvanostatic model in the (I, k_{icc}^0) and $(I, \log k_1^0)$ plane. In the former, the transition from a NDR- to a HNDR-type oscillator can again be seen. Upon varying I, two saddle node bifurcations, but no Hopf bifurcation are encountered for $k_{icc}^0 = 0$, i.e. in the absence of hydrogen contribution. This corresponds to the familiar behavior of potentiostatic oscillators such as the $S_2O_8^{2-}$ reduction in alkaline solution or In^{3+}/SCN^- reduction [213, 172] which are bistable under galvanostatic conditions. Upon increasing k_{icc}^0,the birth of a branch of Hopf bifurcations is discerned. Stable periodic behavior is now bounded by a soft (Hopf) bifurcation and a hard (saddle loop) bifurcation at high
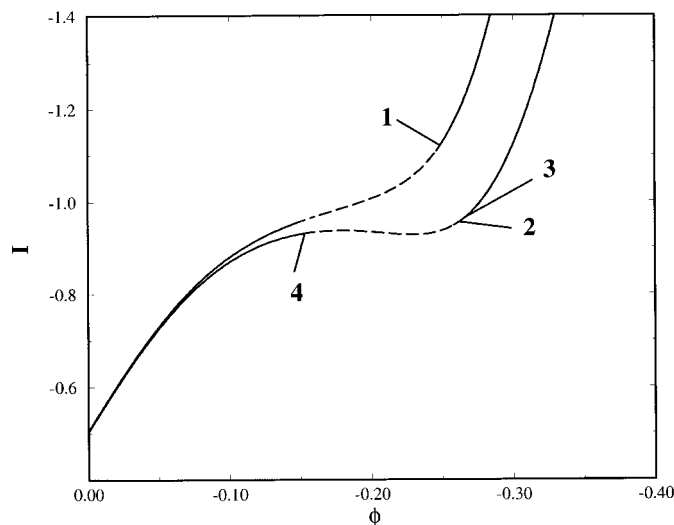
Figure 8-14: stationary I/U profiles and local stability of steady states under galvanostatic conditions, $k_1^0 = 0.01, k_{icc}^0 = 0.3$ (upper graph) 0.8 (lower graph), solid (dashed) lines indicate stable (unstable) steady states. Labels 1 - 4 indicate the steady states on the I/U curves where impedance spectra were calculated.

and low absolute values of I, respectively. Then, a second Hopf line appears followed by the collision of the saddle node bifurcation (cusp bifurcation) until finally at very high hydrogen rate constants the Hopf line turns and disappears, as well. Past the cusp, the model exhibits the behavior of a HNDR oscillator (compare Fig.8-14, upper curve, and Fig.8-10, curve 3 and 4). Fig. 8-20 further reveals that limit cycle behavior is strongly sensitive to the functional form of $k_r(\phi, k_1^0)$. Potential oscillations bounded by two soft (Hopf) bifurcations exist only in a small range of k_1^0 values ($10^{-1.2} - 10^{-1.7}$). Again at smaller k_1^0, stable potential oscillations are bounded by a soft and a hard transition. Interestingly, calculations showed that both saddle-node and Hopf instabilities still exist even for $k_1^0 \longrightarrow 0$. In this limiting case, $k_r(\phi, k_1^0)$ changes its shape from a N to a Λ, i.e. $k_r(\phi, k_1^0) \to 0$ for both $\phi \to \pm\infty$ and therefore exhibits a global rate maximum.

5. Potentiostatic bifurcation behavior The potentiostatic behavior of model A in terms of bifurcation diagrams is depicted in Fig. 8-21 to Fig. 8-23. Fig. 8-21 was calculated at a comparably low resistance and displays only a small range of bistability for positive k_{icc}^0. In contrast to the previous figure, however, the Hopf bifurcation line now extends to $k_{icc}^0 = 0$, since NDR oscillators are able to oscillate under potentiostatic conditions. 8-22 and 8-23 display the dynamics in the (U, ρ) plane at $k_{icc}^0 = 0.0$ and $k_{icc}^0 = 0.3$, respectively, confirming the relation of the shape of the bifurcation diagram to the mechanistic category of the oscillator: Whereas NDR oscillators were reported to exclusively exhibit XPDs, HNDR oscillators usually displayed non-XPD

Figure 8-15: Calculated impedance spectra at the corresponding steady state in Fig. 8-14. Z denotes the total internal impedance of the system.

Figure 8-16: Calculated impedance spectra at the corresponding steady state in Fig. 8-14. Z denotes the total internal impedance of the system.
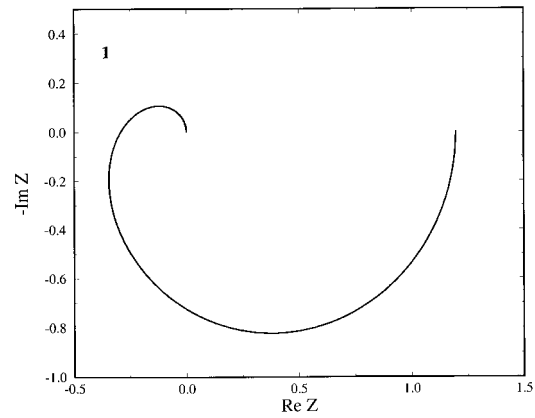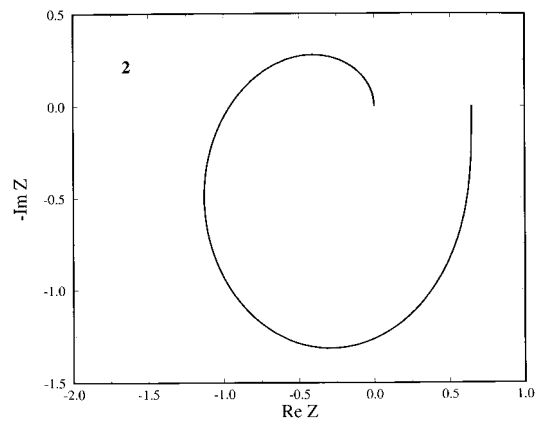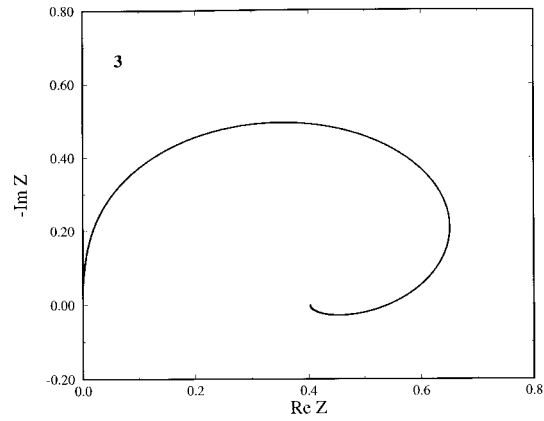
Figure 8-17: Calculated impedance spectra at the corresponding steady state in Fig. 8-14. Z denotes the total internal impedance of the system.
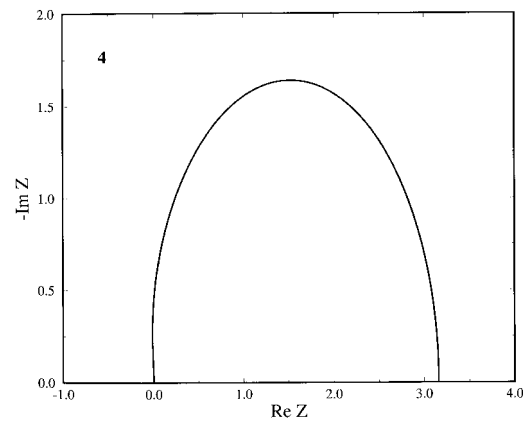
Figure 8-18: Calculated impedance spectra at the corresponding steady state in Fig. 8-14. Z denotes the total internal impedance of the system.

Figure 8-19: Two-parameter bifurcation diagram of model A in the (k_{icc}^0, I) plane with $k_1^0 = 0.01$, dashed line: Hopf bifurcations, solid line: saddle node bifurcations. Within the dashed loop stable limit cycle behavior exists.

Figure 8-20: Two-parameter bifurcation diagram of model A in the (k_{icc}^0, I) plane with $k_1^0 = 0.01$, dashed line: Hopf bifurcations, solid line: saddle node bifurcations. Within the dashed loop stable limit cycle behavior exists.

like diagrams [74]. A clear explanation of the transition has not been given to date. Interestingly, model A allows a smoot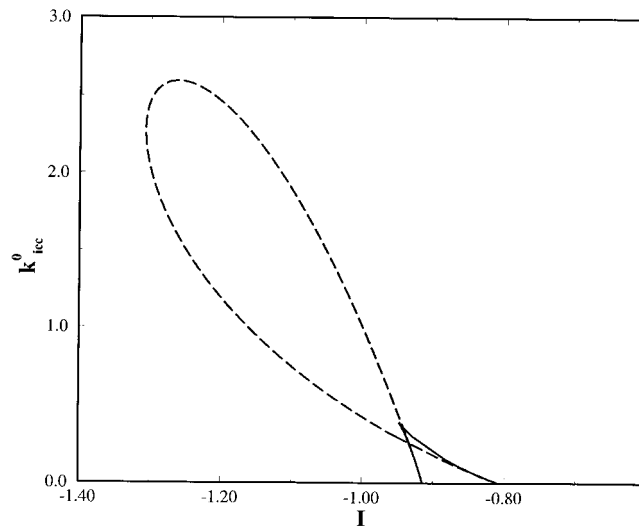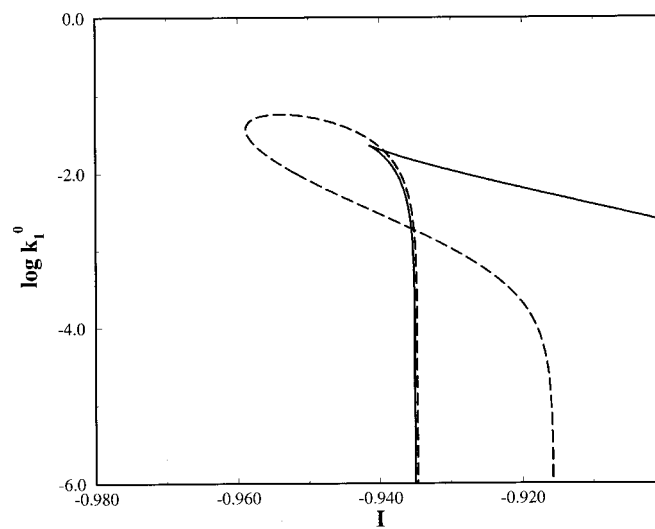h transition from XPD to non-XPD as seen in Fig.8-19 and therefore a study of the changes in the bifurcation diagrams going from a NDR to a HNDR oscillator. Following the changes in the bifurcation diagram with increasing k_{icc}^0, it turned out that both Takens-Bogdanov (TB) points (endpoints of Hopf lines on the saddle node lines) moved towards higher values of U and ρ until one TB point presumably disappeared at infinity while the other remained at very high values of U and ρ. The disappearance of the TB point was associated with the shift of the Hopf bifurcation curve such as to be always located outside the bistable region if followed to infinity (see Fig. 8-23). This potentiostatic features illustrates again a soft and a hard bifurcation for almost all values of the resistance, i.e. also in the limit of $\rho \longrightarrow \infty$, under galvanostatic conditions. Note, however, that the shape of Fig. 8-23 is in contrast to findings in previously investigated potentiostatic oscillators insofar as the relative location of the soft and the hard bifurcation was reversed.
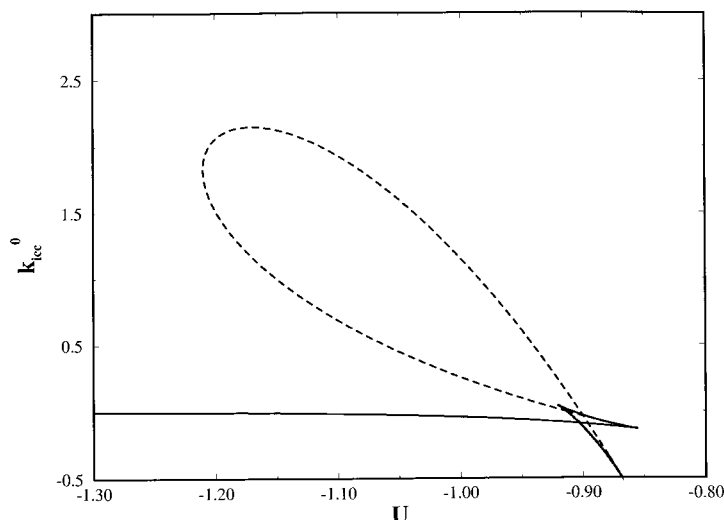
Figure 8-21: Two-parameter bifurcation diagram of model A in the (k_{icc}^0, U) plane with $k_1^0 = 0.01, \rho = 0.8$. Line codings as in previous figures.

6. Phase behavior   Finally, Fig.8-24 illustrates the relative phase behavior of the model variables and the individual faradaic currents at a total current value of $I = -0.95$. Obviously, at high potentials the concentration of iodate drops due to constant fast electron transfer (iodate reduction) which in turn lowers the potential. At a sufficiently low potential, the rate of iodate reduction, i.e. consumption, suddenly drops and the iodate concentration can recover, while the current is carried to a higher percentage by the hydrogen evolution.

Figure 8-22: XPD bifurcation diagram for the NDR case in the (U, ρ) plane with $k_1^0 = 0.01, k_{icc}^0 = 0.0$.

Figure 8-23: Non-XPD bifurcation diagram for the HNDR case in the (U, ρ) plane with $k_1^0 = 0.01, k_{icc}^0 = 0.3$,enlargement (inset) shows the saddle-node bifurcation curves as well the upper Hopf bifurcation curve.

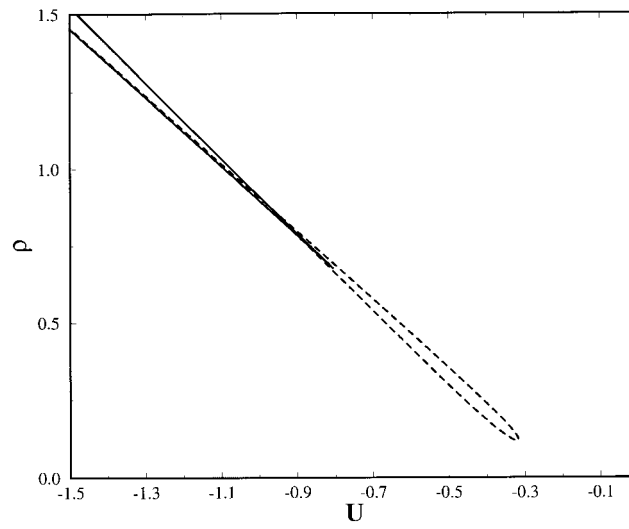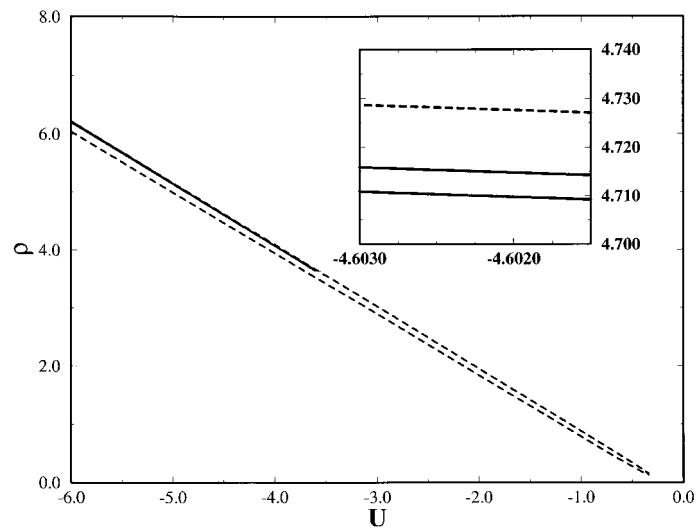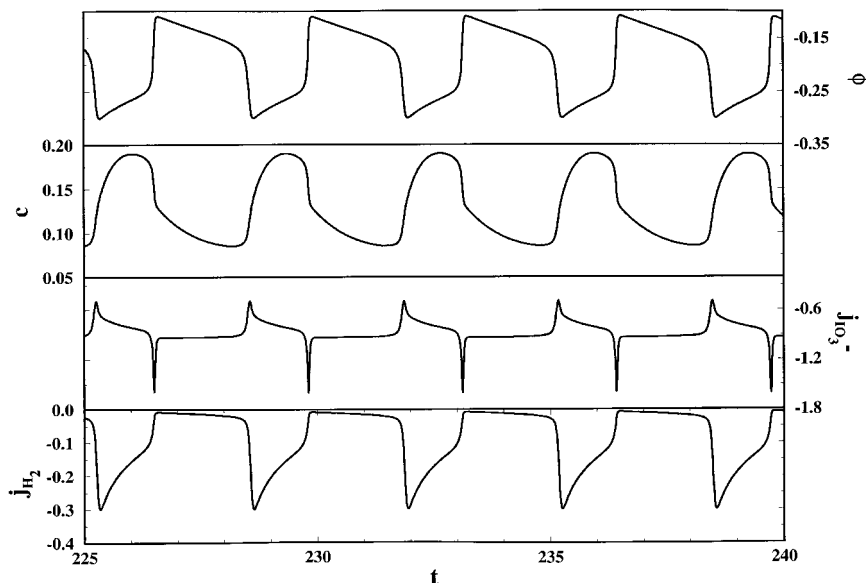Figure 8-24: Relative phase behavior of φ, c, the hydrogen evolution current $j_{H_2} = -k_{icc}^0 \widetilde{k}_{icc}(\varphi)$ and the IO_3^- reduction current $j_{IO_3^-} = -c\, k_r(\varphi, k_1^0)$ using $k_1^0 = 0.01, k_{icc}^0 = 0.3$.

8.4   Discussion

8.4.1   The Iodate Reduction Mechanism

A simple reaction sequence was introduced for the kinetic description of the electrocatalytic iodate reduction which involved (i) a Nernst-type mass transport of the electroactive species IO_3^- between the bulk and the surface [71, 64], (ii) the reduction of IO_3^- to I^- through a single-step or a multi-step reaction sequence (mechanisms A and B) ('dependent' current carrier) and (iii) the presence of an additional 'independent' current carrier coming into effect at lower values of ϕ. Assumption (i) is a very common approximation of the full mass transport problem and has been applied in previous studies [71, 64, 72]. Assumptions (ii) and (iii) followed from the experimental I/U behavior (Fig. 8-1) and respectively from the strong visible hydrogen evolution at higher overpotentials. While the independent current carrier was assumed to exhibit a normal potential regulation throughout, the rate expression of the iodate reduction was chosen to exhibit a non-trivial potential dependence - with the shape of a N (Fig. 8-9) - such as to describe a Frumkin-type repulsion between IO_3^- ions within the diffuse portion of the double layer. The Frumkin hypothesis was supported by a number of experimental findings: Apart from being physically reasonable for the reduction of small anions, the correspondence between the relative location of the potential oscillations on Ag, Au and Pt [30] and the respective

points of zero charge [71, 61] is in favor of Coulomb effects. More importantly, the assumption of a Frumkin effect predicts the autocatalytic nature of ϕ in some potential interval which in turn is associated with a negative real impedance (NDR). The latter was in fact observed in the experimental impedance analysis (Fig. 8-7, 8-6). In particular, Fig.8-7 indicates a NDR on zero-frequency time scale suggesting a slightly negative slope in the stationary I/U characteristic. The impedance findings furthermore justify the choice of the double layer potential ϕ as the fast (autocatalytic) dynamical variable. Usually, when dealing with Frumkin effects, an implicit potential equation for the Frumkin potential [48] has to be solved [71]. The use of a non-monotonous potential dependence of the reaction rate such as $k_r(\phi, k_1^0)$, however, constitutes a common approach to circumvent the tedious solution of implicit equations as reported in calculations using a model of the $S_2O_8^{2-}$-reduction system [214].

Model simulations of (i) potential (Fig. 8-10,8-11,8-12) and current scans (Fig.8-13, 8-14), (ii) bifurcation behavior bounding oscillatory behavior (Fig. 8-19 to 8-23) as well as (iii) impedance spectra were in good qualitative agreement with experiments (Fig. 8-5 to 8-8, compare also Fig.5 in ref.[30]). In particular, the type and the location of bifurcations (soft and hard transition between stable/oscillatory behavior) could be well reproduced.

In contrast to calculations, the experimental impedance plots revealed an additional fast chemical process evidenced by an additional capacitive loop at high frequencies. The unknown process seems to be about two orders of magnitude faster than the characteristic timescale of the oscillatory process (see Fig. 8-4 and impedance measurements). Hydrogen adsorption is unlikely to be responsible for the fast process, since the additional loop was also observable at potentials where no H-adsorption can occur. An extended stepwise reduction mechanism, however, as presented in mechanism B, is able to provide a consistent explanation of the additional capacitive loop. Mechanism B (eq. 8.4) involves an additional intermediate X during the reduction of IO_3^-. As long as the first step is rate determining, the overall kinetics would be governed by reaction 8.4a (low characteristic frequency). Process 8.4b would become visible only on a faster timescale. Since model A involves one chemical species only, it is therefore unable to reproduce a second capacitive loop in the impedance diagrams. In conclusion, the additional fast chemical process in the experimental system leaves all results regarding the mechanistic role of slow chemical process unaffected.

In agreement with previous conjectures [30], the presence of the hydrogen evolution (independent current carrier) turned out to be crucial for the existence of galvanostatic potential oscillations as illustrated in the bifurcation diagram Fig.8-19 or likewise as seen in the analytical analysis of Appendix A. Interestingly, the presence of a positive potential dependence of the dependent current carrier for very large ϕ was shown to be merely a sufficient, but not a necessary condition for galvanostatic oscillatory instabilities, since also a Λ-shaped rate dependence (rate$\rightarrow 0$ as $|\phi| \rightarrow \infty$) resulted in analogous dynamical behavior. Note further, that for large values of k_{icc}^0 ($k_{icc}^0 > 0.4$), the potential oscillations occur at current values above the diffusion limited plateau as reported in [30]. From calculations given in Fig. 8-19 it is obvious that too high a rate of hydrogen evolution can impede the observation of galvanostatic

potential oscillations. Likewise, as shown in 8-20, potential oscillations are very sensitive to changes in the detailed shape of the potential dependence of the dependent current carrier. Thus, Fig. 8-19 and 8-20 show that the existence and the location of galvanostatic oscillations are strongly contingent upon the balance of reaction rates of both the dependent and independent current carrier. Stirring was shown to shift the galvanostatic oscillatory current range to higher current values [30] which is easily explained in the model by the increase of the transport-limited iodate current. The model further predicts that sufficiently strong stirring causes all oscillatory regimes to disappear, since c is fixed at a quasi-constant value and therefore the slow negative feedback variable is removed. This could be verified experimentally.

8.4.2 The origin of the galvanostatic oscillatory instability

Potential oscillations with two current carriers. The central feature of the iodate model is doubtlessly the non-monotonous potential dependence of the iodate reduction rate. $k_r(\phi, k_1^0)$ mimicking a Frumkin interaction of the electroactive species [64], since the condition $\frac{\partial k_r(\phi, k_1^0)}{\partial \phi} > 0$ (inverse regulation) is a precondition for complex conjugate eigenvalues with positive real parts under both potentiostatic and galvanostatic conditions. The negative regulation of $k_r(\phi, k_1^0)$ by itself is the origin of a negative impedance (NDR) in the stationary I/U curve (see Fig.8-10 curve 1). Under galvanostatic conditions, however, a second condition becomes crucial for oscillations. This is the presence of a current carrying process not consuming iodate (independent current carrier): for $k_{icc}^0 = 0$ the galvanostatic model exhibits exclusively bistability (NDR type oscillator), whereas for $k_{icc}^0 > 0$ potential oscillations become possible. Furthermore, at higher values of k_{icc}^0 the NDR becomes hidden (HNDR type oscillator, see Fig.8-10 curve 3,4).

In illustrative terms, the origin of the galvanostatic oscillations can be described as follows: Initially, suppose the value of ϕ is to the right of the relative maximum of $k_r(\phi, k_1^0)$ in Fig.8-9. That is, if the NDR is visible on the stationary I/U characteristic, the value of ϕ is to the right of the relative current minimum of the stationary I/U characteristic (see curve 2 in Fig.8-10). The concentration of iodate at the double layer, c , is steadily depleting, until the limiting current is reached where c becomes zero. If the constant value of I was chosen such as to exceed the limiting current value, ϕ slowly decreases in order to keep up the constant current I. As soon as ϕ enters the region of the negative regulation of $k_r(\phi, k_1^0)$, the NDR leads to an autocatalytic growth of $|\phi|$. As ϕ growths, the rate of iodate reduction drops, whereas the rate of the independent current carrier increases until it balances the difference between I and the instantaneous iodate current. This stops the autocatalytic growth of $|\phi|$. Since the rate of iodate reduction is now around the lower end of the potential region of negative regulation, c has the opportunity to recover as clearly seen in Fig.8-24. A higher value of c leads to a higher diffusion-limited iodate current until it exceeds the chosen value of the total current again. This, in turn, leads to a rise in ϕ and the initial conditions are restored. Note, that without an independent current carrier, the current I would have to be supplied by iodate reduction at all times and no recovery of c would be possible. The potential would remain low and consequently the system would display

bistable behavior (NDR-oscillator). Note that this mechanism is effective regardless whether or not the NDR is visible in the stationary characteristic (NDR or HNDR oscillator).

Potential oscillations with potential-dependent sorption. A similar mechanism operates in the galvanostatic oscillatory prototype model suggested in ref. [64]. There, unlike model A, no additional current carrier is present. Instead, a potential dependent ad- and desorption of the slow chemical species was assumed. Even though the total current I has to be provided by the dependent current carrier at all times, a recovery of the concentration of the chemical species becomes possible due to enhanced adsorption with increasing ϕ.

8.4.3 The bifurcation structure of NDR and HNDR oscillators in the (U,ρ) plane

Whereas Hopf and saddle-node bifurcation sets in NDR oscillators were usually found to exhibit a XPD in some two-parameter plane, this bifurcation structure was always destroyed in HNDR oscillators in favor of some non-XPD. As shown in Fig.8-19, increasing k_{icc}^0 from zero is associated with a continuous transition of model A from a NDR (Fig.8-22) to a HNDR oscillator (Fig.8-23). Therefore, the qualitative changes in the bifurcation structure in the (U/ρ) plane upon increasing k_{icc}^0 could be studied in more detail. It turned out that with larger k_{icc}^0 both TB-points of the XPD moved to higher values of U and ρ until one TB point presumably disappeared at infinity. Simultaneously the Hopf bifurcation curve shifted in such a way that following it in one direction, the curve was located for all $U, \rho \to \infty$ outside the region of bistability (Fig.8-23). This change in location of the Hopf curve enables galvanostatic oscillations. Interestingly, it is not arbitrary which TB point disappears at infinity. Instead, it was found that in models similar to model A, the Hopf bifurcation curve becomes relocated such that the galvanostatic supercritical Hopf bifurcation (Fig.8-13, 8-14 and Fig.8-19, 8-20) is located at large absolute values of I . This is contrast to previous reports in galvanostatic systems and models such as hydrogen oxidation, formic acid oxidation etc. [215, 75, 28] where the galvanostatic soft (Hopf) bifurcation always occurs at small absolute values of the total current, while the hard transition back to stable behavior (mostly saddle-loop bifurcations) occurred at high values of I. That feature, i.e. Hopf at large and hard bifurcation at low values of the total current, seems to be related with the presence of two current carriers and can possibly serve as an experimental criterion for a rapid mechanistic classification of unknown galvanostatic oscillatory systems [69].

8.4.4 Relation to a Convective Mass Transfer Mechanism

In the mechanistic discussions of earlier reports on galvanostatic oscillations during anion reduction reactions such as IO_3^- [30, 208, 209], the authors placed emphasis exclusively on a convective mass transfer feedback mechanism due to hydrogen evolution. In general, potential oscillations involving convective feedback replenishing the concentration of the electroactive species c at the surface require the following assumptions: (i) a diffusion limited current plateau of an electrochemical process, (ii) an

independent current providing process and (iii) a sudden detachment of gas bubbles associated with a very sharp increase of the diffusion limited current by mixing IO_3^-. By means of Fig. 8-25 which schematizes such an oscillatory convection mechanism the origin of oscillations can be understood in detail: As long as the galvanostatically chosen current density I (horizontal line) can be met by the primary electrochemical process (dependent current carrier), the potential remains high (point A). However, constant consumption of the chemical species and slow diffusive mass transport leads to a steady decrease of the current provided by the primary process until it drops below the required value of I. Now, ϕ rises until the current is met by means of the independent current carrier associated with the evolution of gas bubbles (point B). ϕ has reached a low value at this point of the cycle. The bubbling provides a sudden convective force replenishing the concentration c and thereby increasing the diffusion limited current plateau of iodate above the value of I. Note that since this process will eventually restore ϕ, it acts as a negative feedback. Now, the instantaneous value of the iodate current alone exceeds I and consequently ϕ rises until the original conditions are restored. Importantly, if the convective force associated with gas bubbling is on the same or on a smaller timescale as ϕ, sustained periodic behavior is impossible, since a stationary, intermediate potential at moderate bubbling rate will be approached in a damped oscillatory transient. Therefore, sustained periodic behavior requires the unsatisfying assumption of a very sudden bubble-detachment raising the diffusion limited current almost *instantaneously* from an undercritical to an overcritical value.

Sustained regular period-1 oscillations as reported in Fig. 8-2 and 8-3 or ref. [30] require a very high degree of reproducibility of the bubble size as well as of the bubble formation and displacement processes which is unlikely.

Most importantly, however, the mere supposition of one diffusion-limited faradaic current (I_F^{dl}) and an additional independent positively-regulated current ($\hat{I}_F$ where $\left(\frac{\partial \hat{I}_F}{\partial \phi}\right) > 0$) is unable to account for the observed negative real impedances. This is easily shown in a one-species model similar to model A. Since in the diffusion-limited case $\left(\frac{\partial I_F^{dl}}{\partial \phi}\right) = 0$ and $\left(\frac{\partial \dot{c}}{\partial \phi}\right) = 0$ it follows

$$\mathrm{Re}\, Z^{-1} = \left(\frac{\partial \hat{I}_F}{\partial \phi}\right) + \left(\frac{\partial I_F^{dl}}{\partial \phi}\right) - \left(\frac{\partial I_F^{dl}}{\partial c}\right) \frac{\left(\frac{\partial \dot{c}}{\partial \phi}\right)\left(\frac{\partial \dot{c}}{\partial c}\right)}{\omega^2 + \left(\frac{\partial \dot{c}}{\partial c}\right)^2} > 0$$

where all partial derivatives are evaluated in the diffusion-limited stationary state.

In summary, even though it is in principle conceivable for a convective mass transport mechanism to exhibit oscillatory behavior, the experimental findings lend support to an instability mechanism based on a negative impedance rather than to convection-depletion processes.
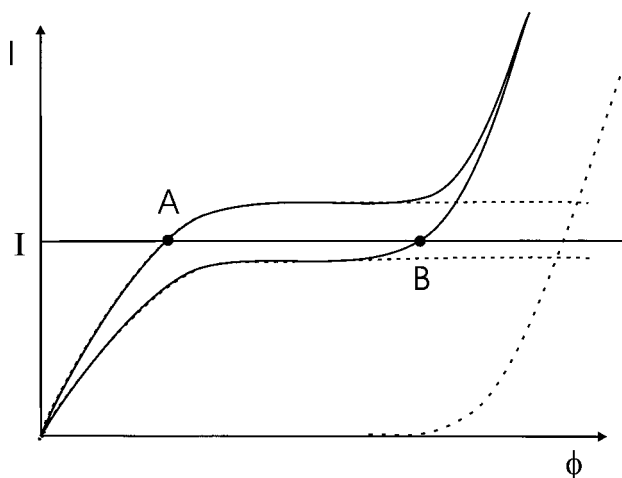
Figure 8-25: Schematic illustration of a possible convection-depletion oscillator under galvanostatic control. The horizontal, solid line shows the constant total current I (see eq.8.6). The two solid plateau curves portray the instantaneous overall I/U behavior immediately before (lower curve) and after (upper curve) evolution of gas bubbles; the respective values of φ (operational points of the system) is given by points A and B. The dashed plateau curves and the dashed exponential curve indicate the individual contributions of the dependent and independent current carrier, respectively.

8.4.5 Extension to other oscillatory electrocatalytic reductions and oxidations

The model and mechanistic considerations introduced above can readily be extended to the description and understanding of further electrocatalytic reduction and oxidation systems (ref. [209] and references therein). An impedance analysis of the $Fe(CN)_6^{3-}$ system [208] , for instance, evidenced the existence of a NDR at finite frequencies suggesting a HNDR type oscillator. In analogy to the iodate reduction system, a Frumkin-type Coulomb interaction appears likely to be the origin of the NDR which, on superposition of an additional current carrier like hydrogen evolution, is able to cause galvanostatic potential oscillations.

The electrocatalytic reduction of $S_2O_8^{2-}$ in alkaline solution is known to be bistable under galvanostatic conditions. In acidic solution, however, potential oscillations are observed. This finding is readily understood if one assumes that the hydrogen evolution in alkaline conditions is shifted too far cathodically to interact with the peroxodisulphate reduction, but approaches the appropriate potential range in order to causes potential oscillations as the pH is lowered.

Potential oscillations were also reported during the electrocatalytic *oxidation* of anions such as $Fe(CN)_6^{4-}$ in the presence of O_2 evolution on Pt electrode [209]. Here, a Frumkin-type interaction of the electrocatalytic species is obviously absent. Note,

however, that the oscillatory potential range coincides with the potential where adsorption of oxygen species [167, 166] occurs. Therefore, a N-shaped potential dependence of the $Fe(CN)_6^{4-}$ oxidation current (similar to Fig.8-9) can be expected simply assuming a lower oxidation rate on Pt which is covered by some oxygen species (Pt-OH or Pt-O) as compared to that on the bare Pt metal surface. In combination with the oxygen evolution current, a HNDR oscillator is obtained just like the one introduced above.

8.5 Summary

A kinetic two-variable model for the oscillatory iodate reduction under galvanostatic control was shown to explain numerous experimental features previously unaccounted for. The essential parts of the model consisted, first, in a non-monotonous potential dependence of the major current carrier (iodate reduction) which was associated with a NDR and, second, in an independent current carrier with normal potential regulation (hydrogen evolution). This combination resulted in a novel type of galvanostatic oscillatory models (subclass of the HNDR category) with which among other things the transition from a NDR to a HNDR oscillator could be studied. The origin of the instability was discussed in the context of previous suggestions. The mechanism of the oscillatory instability was shown to be also applicable to a whole class of related electrocatalytic galvanostatic oscillators.